

Structure of and ion segregation to an alumina grain boundary: Implications for growth and creep

Ivan Milas, Berit Hinnemann,^{a)} and Emily A. Carter^{b)}

Department of Mechanical and Aerospace Engineering, Princeton University, Princeton, New Jersey 08544-5263; and Program in Applied and Computational Mathematics, Princeton University, Princeton, New Jersey 08544-5263

(Received 10 January 2008; accepted 26 February 2008)

Using periodic density-functional theory (DFT), we investigated the structure and cohesive properties of the α -alumina Σ 11 tilt grain boundary, with and without segregated elements, as a model for the thermally grown oxide in jet engine thermal barrier coatings. We identified a new low-energy structure different from what was proposed previously based on electron microscopy and classical potential simulations. We explored the structure and energy landscape at the grain boundary for segregated Al, O, and early transition metals (TMs) Y and Hf. We predict that the TMs preferentially adsorb at the same sites as Al, while some adsites favored by O remain unblocked by TMs. All segregated atoms have a limited effect on grain boundary adhesion, suggesting that adhesion energies alone cannot be used for predictions of creep inhibition. These findings provide some new insights into how TM dopants affect alumina growth and creep kinetics.

I. INTRODUCTION

Jet turbine engines operate at temperatures higher than the melting point of the Ni-based superalloy used for many of the engine parts. This feat is accomplished via the use of a thermal barrier coating (TBC), which acts as a heat shield to reduce the effective temperature experienced by the underlying alloy. A typical TBC consists of three layers: (i) a NiAl-based bond coat alloy deposited on the Ni superalloy substrate to improve TBC adhesion and provide an abundant source of Al, (ii) a yttria-stabilized zirconia (YSZ) topcoat for thermal protection, and (iii) a thin layer of a thermally grown oxide (TGO) in between, the purpose of which is to protect the superalloy from oxidative corrosion, since oxygen readily diffuses through the YSZ layer. Alumina (Al_2O_3) is the optimum TGO, as it has the lowest oxygen mobility of all oxide ceramics up to very high temperatures, thereby providing corrosion protection, while having a relatively slow oxide growth rate.^{1,2} This slow growth rate is critical, since thermal cycling produces stresses due to the coefficient of thermal expansion mismatch between alumina and the metal alloy. Once the TGO grows past a critical thickness (typically $<10\ \mu\text{m}$), the stress build-up is so large that the coating spalls.³ Hence, a key to

extending the lifetime of TBCs is to slow down the TGO growth rate.

The high temperatures experienced by TBCs produce a constantly evolving coating composition controlled by atomic diffusion. In particular, inward diffusion of oxygen from the air through the YSZ layer and outward diffusion of aluminum from the bond coat alloy react at the metal–oxide interface to form α -alumina. Hence oxygen and aluminum diffusion kinetics directly control the rate of thickening of the alumina layer.

Despite an abundance of recent experimental and theoretical investigations,^{4–13} diffusion mechanisms in α -alumina are not well understood, because of scatter in available data. One problem is the strong dependence of oxide properties on impurity content (manufacturing highly pure α -alumina is very difficult), which gives rise to sometimes inconsistent observations.⁴ Most measurements indicate that aluminum and oxygen diffusion rates along α -alumina grain boundaries (GBs) are larger than those in bulk alumina.^{5–8,14,15} However, some recent measurements implied that diffusion along GBs involves higher activation energies than in bulk, which could in turn imply lower rates along GBs, depending on the value of the pre-exponential factors.⁹ Early on, Oishi and Kingery compared self-diffusion of oxygen in single-crystal and polycrystalline α -alumina samples using ^{18}O isotope tracer studies.¹⁴ Their diffusion rates through polycrystals were nearly two orders of magnitude larger than through single crystals due to lower diffusion activation energies. About ten years later, Kitazawa and

^{a)}Present address: Haldor Topsøe A/S, Nymøllevej 55, DK-2800 Lyngby, Denmark.

^{b)}Address all correspondence to this author.

e-mail: eac@princeton.edu
DOI: 10.1557/JMR.2008.0188

Coble used conductivity measurements to study point defect diffusion in two α -alumina polycrystals with differing grain sizes.¹⁵ They also found diffusion rates in polycrystals to be higher than those measured in single crystals. Moreover, the polycrystalline sample with smaller grains, and hence a greater GB area, exhibited a higher diffusion rate, again consistent with the notion that GB diffusion dominates.

More recent experiments by Pan et al. measured self-diffusion activation energies in single crystal and polycrystalline α -Al₂O₃ at 400–1000 °C by impedance spectroscopy.⁹ Their experiments on polycrystalline alumina registered increases in the diffusion activation energy as the grain size decreased, implying that activation energies for diffusion along GBs are higher than for bulk. These latter observations may still be consistent with higher overall rates, when one considers the experiments of Monty and coworkers,^{5–8} who examined self-diffusion of oxygen and aluminum in α -Al₂O₃ single and polycrystals, using ¹⁸O and secondary ion mass spectrometry. Above 1460 °C, they found that oxygen diffusion along GBs is favored over bulk diffusion, despite having higher activation energies, because of favorable preexponential factors. Thus the conclusion from the more recent experimental data seems to be that diffusion rates along GBs are higher, despite possible higher diffusion activation energies. However, the accuracy of the activation energies and preexponential factors obtained by Monty and coworkers was challenged by Harding et al.¹¹ They argued that the limited temperature range spanned in the experiments caused errors in the fit of the Arrhenius plots, which led to unreasonably high and inaccurate activation energies and preexponential factors. More measurements of tracer diffusion in polycrystalline alumina over a wide temperature range is clearly needed to reach consensus.

The addition of reactive elements (REs) like Y, Hf, Zr, and La to the bond coat alloy has been observed to slow the growth of the alumina layer.¹⁶ Wright and Pint showed that the presence of REs changes the predominant alumina growth mechanism, as inferred from a change in the oxide morphology.¹⁷ Since REs have been observed to readily segregate to certain GBs,¹⁸ Pint argued that by doing so they may block the most energetically favorable diffusion route for aluminum atoms and hinder their outward diffusion. As a result, the rate-determining step would become the slower inward diffusion of O atoms.¹⁶ A similar effect is seen in tensile creep experiments of RE-doped α -alumina at high temperatures, where the REs that have segregated to GBs cause a multifold decrease in the creep rate.¹⁹ Since the creep rate is generally associated here with the diffusion rate of elements in the oxide, REs have been suggested to act as blockers of aluminum diffusion pathways at GBs.^{20,21} All these findings support the fact that GBs

play a very important role in diffusion processes in α -alumina and that characterizing the diffusion pathways, energetics, and kinetics involved, along with the effect of REs on diffusion kinetics, may be key to controlling growth of the thermally grown oxide layer.

Before embarking on a detailed study of element diffusion at GBs, the structures of the GBs must be characterized. High-resolution transmission electron microscopy (HRTEM) tends to be the technique of choice for investigating GBs in α -Al₂O₃.²² Rühle and coworkers used HRTEM with a resolution of 0.12 nm to investigate the Σ 13,²³ as well as the symmetric tilt (10 $\bar{1}$ 1) and ($\bar{2}$ 116)²⁴ and the near tilt (10 $\bar{1}$ 1) \parallel (10 $\bar{1}$ 1)²⁵ Σ 11 GBs in α -alumina. These GBs were created by artificially forming bicrystals by attaching two precisely cut surfaces by diffusion bonding. In all cases, the HRTEM micrographs were interpreted by comparing them to structures obtained with static-lattice calculations using an ionic classical potential model. We review their findings only for the near tilt Σ 11 GB, as we have selected it for further study in the present work. Of the three structures calculated for the Σ 11 GB, the structure with the lowest GB energy (according to the classical potential model) also most closely resembled the micrograph. A relatively high density of atoms at the GB was inferred, with the atoms at this Σ 11 GB assembled in such a way as to minimize the void spaces at the interface, while keeping like-charged ions away from each other.

On the basis of these findings,²⁵ Kenway constructed a 180-atom model of the Σ 11 GB and used three different empirical potentials to optimize the model's structure and to calculate GB and adhesion energies.²⁶ French and coworkers further analyzed his model using a non-self-consistent adaptation of the orthogonal linear combination of atomic orbitals (OLCAO) method within the local density approximation (LDA) of density-functional theory (DFT) to calculate charge distributions and local densities of states (LDOS) of atoms at the GB.^{27,28} After further structure optimization, French and coworkers loosely divided the structure into three regions based on ion coordination and bond lengths: (i) within 3 Å on either side of the GB, atoms were under-coordinated and had bond lengths differing from bulk alumina by up to 0.2 Å, (ii) further away, an interior region closely resembled bulk alumina, and (iii) a third region consisted of atoms on the outer surface.

The most extensive theoretical study to date of ion segregation at α -alumina GBs was done by Elsässer and coworkers, who used DFT within the LDA to investigate the rhombohedral Σ 7 ($\bar{1}$ 012),²⁹ the prismatic Σ 3 (10 $\bar{1}$ 0),³⁰ and the pyramidal Σ 13 (10 $\bar{1}$ 4) twin GBs.^{30,31} They first determined the lowest energy structures of those GBs, including the optimal surface terminations. They then focused on the effect of cation impurities on the structure, electronic states, and energetics of these twin GBs.

The RE effect was studied by characterizing structural changes and the segregation energy when an impurity cation was substituted for an aluminum cation at the GB interface. The segregation energy was obtained by comparing the sums of the total energies of the GB and bulk alumina models for the two cases in which one or the other contained the impurity cation. They found a direct correlation between the ionic radius and the propensity for segregation (i.e., larger cations exhibited more exothermic segregation energies). For certain GBs, the presence of Y and La cations at the interface made the GB more stable than bulk alumina with the same impurity. Furthermore, the authors proposed that the lower energy is driven only by the “segregant size effect,” since the character of the bonds formed between the impurity atom and the neighboring oxygen atoms at the GB are very similar to the ones found for the impurity in bulk α -alumina. The same effect (larger cations exhibiting larger segregation enthalpies) was predicted earlier by Cho et al. using empirical pair potentials.³² They identified possible segregation sites at the $\Sigma 3$ tilt and the $\Sigma 13$ basal alumina GBs by calculating the void volume distribution at the GBs and comparing it to the ionic radii of various dopants.

In the present work, we used DFT with projector-augmented wave (PAW) all-electron frozen-core potentials within the generalized gradient approximation (GGA) for exchange-correlation to revisit characterization of the structure and electronic properties of the $\Sigma 11$ ($10\bar{1}\bar{1}$)||($10\bar{1}1$) GB. Although a large number of different GBs form simultaneously during α -alumina growth, we selected one representative GB to examine in detail. Such high symmetry GBs as the $\Sigma 11$ undoubtedly represents only a very small segment of the GB population, but we hope that the qualitative insights gleaned by a detailed study of one GB may apply more generally.

After structural characterization, we determined the favorable adsorption sites for Al, O, Y, and Hf atoms at the GB, evaluating segregation energetics and GB strength as a function of impurity type. The calculation methodology is presented in Sec. II. Optimized structures, charge density difference maps, preferred ion adsorption sites, segregation energies, and GB adhesion energies are discussed in Sec. III. These findings are analyzed in the context of previous work and their implications for TBC stability are provided in Sec. IV, while key conclusions are summarized in Sec. V.

II. CALCULATIONAL DETAILS

A. Grain boundary characterization

We performed Kohn–Sham DFT^{33,34} calculations within the Vienna Ab Initio Simulation Package (VASP),^{35–37} which imposes periodic boundary conditions and employs a plane wave basis. The valence

electron-ion (nucleus plus core electron) interaction is described using Blöchl’s PAW formalism,³⁸ as implemented by Kresse and Joubert.³⁹ The Perdew–Burke–Ernzerhof (PBE)⁴⁰ GGA functional was used to describe electron exchange and correlation.

Plane wave basis kinetic energy cutoffs of 400 eV for the valence wavefunctions and 610 eV for the augmentation density were used for all ion relaxation calculations. After each structural optimization, a subsequent calculation was performed with a valence wavefunction kinetic energy cutoff of 530 eV to obtain more accurate total energies. Test calculations for the pristine GB and with each type of dopant present showed that the optimized geometry was not appreciably affected by using the higher cutoff (structural changes of <0.1 Å occurred), so structures were not re-optimized at the higher cutoff. However, optimization of the bulk lattice vectors by stress minimization was done with a valence wavefunction kinetic energy cutoff of 530 eV to calculate accurate values for the stress tensor.

The Brillouin zone was sampled with a Γ -point-centered grid of $1 \times 4 \times 1$, using the Monkhorst–Pack scheme,⁴¹ which corresponds to spacings of 0.457, 0.369, and 0.184 \AA^{-1} along the a , b , and c lattice vectors, respectively. The k -point mesh and the 400 eV/610 eV kinetic energy cutoffs above produce total energies converged to 0.002 eV/atom. Their convergence for alumina surfaces is described elsewhere,⁴² but this mesh is sufficient to converge the total energies of the 180+-atom unit cells we use here.

All results for the pristine GB were obtained by spin-restricted calculations, since all electrons in alumina are paired and all structures we consider are stoichiometric, i.e., they contain an integer number of Al_2O_3 formula units. Segregation of reactive elements on the GB interface was done with spin-polarized calculations due to the open-shell nature of these dopants. Ion relaxations were performed with a conjugate gradient algorithm and the forces on each atom were converged to 0.03 eV/\AA .

Because of various possible surface terminations and relative translations of the constituent surfaces, a large number of potential $\Sigma 11$ ($10\bar{1}\bar{1}$)||($10\bar{1}1$) GB structures exist. A first principles survey of such a large number of structures is not viable; one has to restrict the pool of structures considered. As a starting point, we use the model constructed by Kenway for the $\Sigma 11$ ($10\bar{1}\bar{1}$)||($10\bar{1}1$) GB, based on HRTEM images and his own calculations using empirical potentials.²⁶ We therefore used the same surface terminations as described in the Kenway model throughout our work and then conducted a survey of relative translations to search for low energy GB interfaces. The terminations of both surfaces involved are characterized by a concatenation of Al and O atoms distributed in a zig-zag fashion, with O atoms

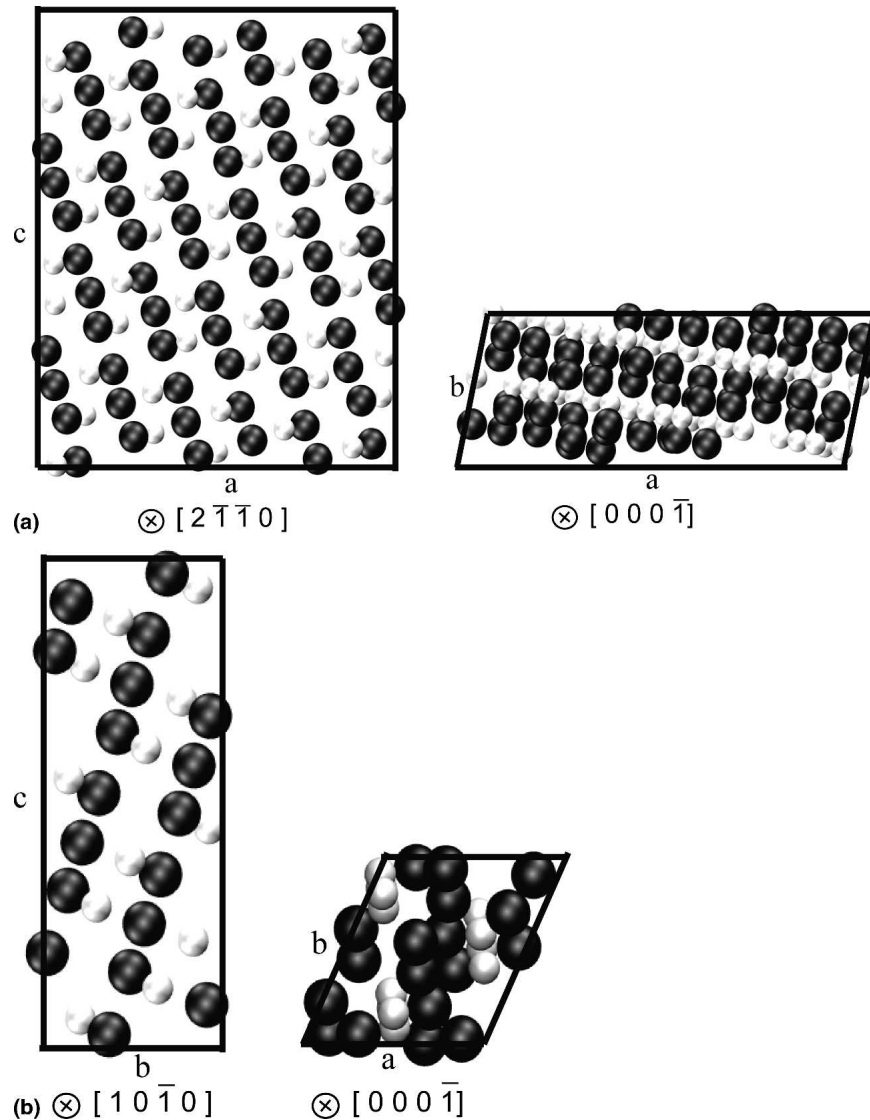


FIG. 1. Optimized geometries for the: (a) (10 $\bar{1}\bar{1}$) surface and (b) (10 $\bar{1}\bar{1}$) surface. The oxygen atoms are represented in black and the aluminum atoms in white. Side views on the left, top views on right. The [2 $\bar{1}\bar{1}0$] direction is in the plane of the (10 $\bar{1}\bar{1}$) surface, while the [000 $\bar{1}$] direction is normal to the (10 $\bar{1}\bar{1}$) surface for (a). The [10 $\bar{1}0$] direction is in the plane of the (10 $\bar{1}\bar{1}$) surface. The [000 $\bar{1}$] direction is normal to the (10 $\bar{1}\bar{1}$) surface in (b).

alternating in the top and bottom positions, as shown in Figs. 1(a) and 1(b).

After adopting the Kenway model termination, we needed to determine a converged thickness for the GB slab model to ensure that no artifacts are introduced by finite slab thickness or vacuum layer thickness that separates the periodic images of the slab used. Here we use a vacuum thickness of 10 Å, which tests showed to be sufficient to prevent interactions between periodic images of the slab. The thickness of each side of the GB has to be large enough to correctly describe interface properties, such as structure, bonding, and energetics, while keeping computational costs reasonable. The criterion we used to determine the optimal thickness for each side of the GB was the convergence of the surface energy S , defined as

$$S = \frac{(E_{\text{surface}} - n \cdot E_{\text{bulk}})}{2A} \quad (1)$$

E_{surface} is the total energy of a slab containing n stoichiometric Al₂O₃ formula units that represents one side of the GB. E_{bulk} is the total energy of the bulk unit cell per stoichiometric formula unit of Al₂O₃ and A is the area of one surface of the slab.

We calculated optimized structures for both surfaces comprising the GB while increasing the thickness of each slab from three through six stoichiometric layers. We define a layer as the thinnest possible surface slab cut in the direction parallel to the surface that contains a stoichiometric proportion of O and Al atoms. In the case of the (10 $\bar{1}\bar{1}$) surface, a layer contains 10 atoms, whereas

the $(10\bar{1}\bar{1})$ surface has a larger lateral unit cell and therefore a layer contains 30 atoms (Fig. 1). In both cases, each layer has a thickness of approximately 3.94 Å. As usual for surface energy calculations, the ions were fully relaxed, while the lattice vectors of the surface unit cell were not optimized but were held fixed at those optimal for bulk alumina, where the bulk lattice vectors were optimized at the same level of theory used for the surfaces and GBs reported here.⁴²

After determining the required thickness of each side of the GB, we then constructed the Kenway model as described in Ref. 26 and used it as the starting point to construct a periodic unit cell model of the GB. Figure 1 illustrates that the unit cell area of the $(10\bar{1}\bar{1})$ surface is much larger than that of the $(10\bar{1}1)$ surface. The bulk-derived lattice vectors for the $(10\bar{1}\bar{1})$ surface are $a = 13.969$ Å and $b = 4.809$ Å, whereas the $(10\bar{1}1)$ surface has $a = 5.149$ Å and $b = 4.809$ Å. Fortunately, the unit cells differ in the magnitude of only one of the vectors, thus by replicating the shorter unit cell three times in the a direction, we obtained a fair match. However, the surfaces still did not coincide perfectly, as the new $(10\bar{1}1)$ surface unit cell is: $a = 15.537$ Å and $b = 4.809$ Å. We then expanded the shorter lattice vector for the $(10\bar{1}\bar{1})$ surface to match the larger one for the $(10\bar{1}1)$ surface. Alternatively, we could compress the larger vector to the length of the shorter one. Test calculations for this latter structure demonstrated that the compressed structure is higher in energy by 1.58 eV after ion relaxation compared to our optimized Kenway model

structure. We therefore decided to use the former structure (one side in tension, rather than compression). We also performed a lattice vector optimization along with ion relaxation, but no significant differences in the lattice vectors' magnitude or orientation were found. The a vector changed by 0.022 Å and the b vector by 0.038 Å. We therefore did not optimize the lattice vectors in subsequent calculations but kept the lattice vectors at those derived from bulk α -alumina. Complete ion relaxation was performed in all calculations (i.e., no ions were held fixed in bulk positions).⁴²

The next step was to check for the existence of structures with a lower total energy than that obtained by ion relaxation of the Kenway model. To this end, we considered alternative relative translations of the two surface slabs contained in the unrelaxed Kenway model. This was done by translating the $(10\bar{1}\bar{1})$ surface relative to the $(10\bar{1}1)$ surface along the vectors a and b . Since the $(10\bar{1}1)$ surface is composed of three unit cells repeated along the lattice vector a , it is sufficient to perform the scan along only one third of the lattice vector a . A potential energy surface scan was then constructed by performing single-point energy calculations (i.e., no ion relaxation) of the 38 structures, as shown in Fig. 2. In a second step, we selected 11 structures with energies within 2.5 eV of the minimum and performed full ion relaxation.

For these optimized structures, we then calculated the GB adhesion energy as

$$E_{\text{adh}} = \frac{E_{\text{GB}} - (E_{10\bar{1}\bar{1}} + E_{10\bar{1}1})}{A}, \quad (2)$$

where E_{GB} is the total energy of the GB slab, and $E_{10\bar{1}\bar{1}}$ and $E_{10\bar{1}1}$ are the total energies of the lowest energy structures of the two surface slabs and A is the area of the GB interface. A negative value for the adhesion energy implies that the GB is more stable than the separated surfaces. The surface slab energies were obtained by cleaving the total structure along the GB plane and then performing full ion relaxation for each surface slab, while keeping the lattice vectors fixed. The surface area of $(10\bar{1}\bar{1})$ in this case will correspond to the GB interface area and not the minimum energy one with its smaller a lattice vector. This is done so as to eliminate strain energy contributions, which will not be evaluated correctly given the length scale mismatch between the atomic scale model (nm) and an actual grain size (microns).

We also calculated the GB energy, defined as

$$E_{\text{int}} = \frac{E_{\text{GB}} - n \cdot E_{\text{bulk}}}{A}, \quad (3)$$

where E_{GB} is the total energy of the GB slab, n is the number of stoichiometric Al_2O_3 formula units, and E_{bulk} is the total energy per stoichiometric formula unit of bulk α - Al_2O_3 .

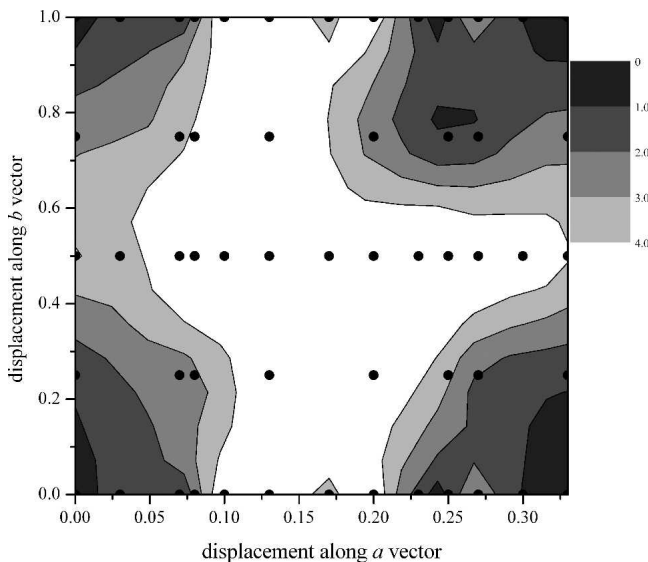


FIG. 2. Potential energy surface for lateral translation scan. Dots represent 38 points at which single-point energy calculations were performed. The translation vector is represented in direct lattice coordinates. The energies of the structures are displayed in eV and are relative to the energy of the global minimum. The regions that differ from the global minimum by more than 4 eV are displayed in white.

To gain insight into chemical bonding at the GB, electron density differences were calculated and plotted for the three lowest energy structures. The electron density difference is defined as

$$\Delta\rho = \rho_{\text{GB}} - (\rho_{(10\bar{1}\bar{1})}^{\text{frozen}} + \rho_{(10\bar{1}1)}^{\text{frozen}}) \quad , \quad (4)$$

where ρ_{GB} is the optimized electron density of the GB, while $\rho_{(10\bar{1}\bar{1})}^{\text{frozen}}$ and $\rho_{(10\bar{1}1)}^{\text{frozen}}$ are the optimized electron densities of the $(10\bar{1}\bar{1})$ and the $(10\bar{1}1)$ surfaces, respectively, with the positions of the atoms kept frozen to those of the optimized GB structure. In this way, we can isolate how the electrons rearrange due to the presence of the GB.

The coordination number of atoms throughout this work was determined based on the number of atoms of opposite charge within a radius of 2.5 Å. This radius is slightly larger than the equilibrium lengths of Al, Y, and Hf bonds to oxygen in their respective bulk oxides, to include partial or elongated bonds that could form at the GB interface that are still within the nearest-neighbor shell.

B. RE Segregation

After determining the minimum energy structure for the $\Sigma 11 (10\bar{1}\bar{1})|(10\bar{1}1)$ GB, we sought to locate all stable adsorption sites at the GB for Al, O, Y, and Hf atoms, as a first step toward investigating diffusion pathways at this GB. The same methodology used for the pristine GB was utilized for RE adsorption calculations, including the same k-point mesh, plane wave kinetic energy cutoffs and convergence criteria. The only difference was that these calculations were done within spin-polarized DFT to allow open-shell character on the impurities and nearby atoms to develop if preferred.

We placed neutral, ground state, adsorbate atoms at GB interstitial sites (spin doublet states for Al and Y, spin triplet states for O and Hf). In this way, we maintain overall charge balance, eliminating the need to create vacancies or an artificial homogeneous compensating charge background to retain electrostatic neutrality.²⁹ Furthermore, the actual charge states of the REs at the GB are not known; thus the charge requiring neutralization is not clearly defined. Based on the findings of Hinemann and Carter for adsorption of REs on $\text{Al}_2\text{O}_3 (0001)$,⁴² these initially neutral atoms are expected to partially ionize as they interact with other ions along the GB interface. Since these atoms begin as neutral species before entering the GB (either from air or metal), we posit that adding them initially as neutral species is reasonable.

The adsorption sites were identified in the following manner. First, the GB interface was scanned for potential adsorption sites by placing an adsorbate atom at 40 different positions on the GB interface and

performing a single-point energy calculation (no ion relaxation). Second, for the lowest energy structures, we then allowed the adsorbate atom to relax. Last, relaxation of the whole structure was performed and the adsorption site characterized. We calculated the vibrational frequencies from the eigenvalues of the Hessian (energy second derivative) matrix to verify if the structures are indeed local minima and not saddle points. The Hessian was evaluated numerically from finite differences of analytic gradients by displacing all atoms within 3.0 Å of the adsorbed atom by 0.02 Å along the three Cartesian coordinate axes. The frequencies of all vibrational modes around the adsorbate were real and larger than 100 cm^{-1} , proving that the structures are indeed local minima. Displacements of 0.01 and 0.03 Å were tested also and produced similar frequencies. RE-oxo bond lengths and the coordination numbers at the GBs were analyzed also, to understand the trends observed.

The adhesion energies for the GB structures with the adsorbates were calculated using the same expressions and procedure described above for the pristine GB. One adsorbate per unit cell corresponds to an adsorbate coverage at the GB of 0.17 monolayers (ML), which is lower than, e.g., the average yttrium coverage found in alumina GBs (0.25–0.5 ML).^{43,44} Higher coverages were also considered by adding more than one adsorbate per GB unit cell, as discussed below. One monolayer is defined here as a 1:1 ratio of RE atoms to surface Al atoms on one side of the GB. Two values for the adhesion energy were obtained for each adsorbate since the adsorbate could be on either surface as the GB is pulled apart. To obtain the most conservative estimates, the GB adhesion value associated with the lowest energy pair of surfaces, and thus lowest adhesion energy, was taken as the final GB adhesion energy estimate.

To assess the effect of increasing coverage of REs at this $\Sigma 11$ GB, the segregation energies for multiple Y and Hf atoms moving to the GB were also calculated. The maximum RE concentration at the GB interface should give additional insights into the extent to which REs may affect diffusion rates along the GB. We define the segregation energy of the n^{th} RE atom as

$$E_{\text{seg}}(n) = \frac{E_{\text{GB},n} - E_{\text{GB},n-1}}{A} \quad , \quad (5)$$

where $E_{\text{GB},n}$ is the total energy of the system with n RE atoms segregated to the GB. $E_{\text{GB},n-1}$ is the total energy of the system in which the position of one of the n RE GB atoms is exchanged with an aluminum atom from the middle of the unstretched side of the grain boundary, since it is the most bulk-like part of the slab model. The sign of the segregation energy indicates whether it is

thermodynamically more favorable for the n th RE atom to segregate to the GB or to remain in the bulk, if $n - 1$ RE atoms are already segregated to the GB. A negative value means that the n th RE atom will preferentially segregate to the GB.

III. RESULTS

A. Grain boundary characterization

Our first task was to determine the minimum thickness of each of the surface slabs that yields a converged value for the surface energy, while avoiding model artifacts. Ion relaxation with three stoichiometric layers for both surfaces—i.e., 90 atoms for the $(10\bar{1}1)$ surface and 30 atoms for the $(10\bar{1}\bar{1})$ surface—yields surface energies of 1.80 J/m^2 and 2.08 J/m^2 , respectively. Adding extra layers beyond three causes variations of only a few mJ/m^2 in the surface energy (Table I). In particular, these values are converged at three layers to within 0.011 and 0.002 J/m^2 for the $(10\bar{1}1)$ and $(10\bar{1}\bar{1})$ surfaces, respectively. Hence, the three-layer-thick surface slabs seem adequate for construction of the GB. Thus, after replicating the smaller $(10\bar{1}1)$ cell three times to approximately match the lateral cell size of the larger $(10\bar{1}\bar{1})$ cell, we obtain a GB model of 180 atoms, the same size as Kenway constructed.

After determining the converged size of the supercell model, we determined the optimal GB structure. The geometry optimization was performed in two steps. First, we calculated the energies of frozen structures obtained by translating the top crystal slab relative to the bottom one along the a and b vectors of the GB interface, without ion relaxation. The zero lateral translation $(0.0, 0.0)$ corresponds to the unrelaxed Kenway model structure. The results obtained are depicted in Fig. 2. In this figure, the black dots represent the 38 sampling points of the potential energy surface and the shades of gray represent the energy of each structure relative to the energy of the unrelaxed Kenway model. The spacing between the points is at most 1 \AA , which is much smaller than the length of the average Al–O bond in alumina (1.9 \AA). This ensures that possible minima on the potential energy surface are not overlooked in the scanning process.

The second step is to select a number of low energy structures and to allow full ion relaxation of those structures. The frozen structure energies of all sampled structures lie in a range of $\sim 7 \text{ eV}$, with a gap in the distribution of low energy structures at $\sim 2 \text{ eV}$. We therefore selected all frozen lowest energy structures whose energies were within the $0\text{--}2 \text{ eV}$ range as candidates for ion relaxation. Twelve such structures qualified, with the relaxed Kenway model structure now found to be second lowest in energy, but only higher than the lowest energy structure by 1 meV at this stage.

We then allowed full ion relaxation of those 12 structures (Table II). The structure obtained by relaxing the

TABLE I. Convergence of surface energies (J/m^2) for the $(10\bar{1}1)$ and $(10\bar{1}\bar{1})$ free surfaces as the number of stoichiometric Al–O₃–Al layers of each is increased.

Number of layers	Surface energy (J/m^2)	
	$(10\bar{1}1)$	$(10\bar{1}\bar{1})$
3	1.801	2.083
4	1.810	2.083
5	1.808	2.081
6	1.812	2.083

TABLE II. Interface and adhesion energies (J/m^2) for the two GB structures found to be lowest in energy, as well as for the relaxed Kenway model structure. Lower interface energy and more negative adhesion energy indicate greater stability.

GB structure	Interface energy (J/m^2)	Adhesion energy (J/m^2)
Kenway model/ $(0.0, 0.0)$	7.69	-1.31
$(0.23, 0.0)$ structure	6.92	-2.08
Global minimum $(0.0, 0.25)$	6.60	-2.40

Kenway model was only the fifth lowest in energy and 5.05 eV higher in total energy per unit cell than the global minimum. The GB interface and adhesion energies of the global minimum structure are respectively lower (easier to form from single crystal α -alumina) and higher (grains more strongly adhered) by 1.09 J/m^2 than the optimized Kenway model. Our new structural prediction based on self-consistent all-electron DFT-GGA theory should be more reliable, since the Kenway model structure optimized by French and coworkers in 1994 was derived from a non-self-consistent DFT calculation, using an effective potential derived from bulk alumina.

Our optimized Kenway model structure is compared to our predicted two lowest energy structures in Figs. 3(a)–3(c). All three structures display the same overall characteristics: planes of oxygen atoms at angles of $\sim 73^\circ$ to the interface plane and a zig-zag fit of the two surfaces. Differences lie in the distribution of atoms and bonding at the GB interface. The Kenway model displays sizeable voids in the GB region, whereas our predicted global minimum energy structure has a GB region with smaller voids and more uniformly filled spaces.

Our two lowest energy minima are obtained from relaxation of structures very similar to the Kenway model. The global minimum corresponds to a structure that is shifted from the Kenway model by 0.25 in fractional coordinates or 1.20 \AA in the direction of the b vector of the supercell. The structure with the second lowest energy is obtained by translating the top surface by 0.23 in fractional coordinates or 3.57 \AA in the direction of the a vector of the supercell. Although the Kenway model appeared to fit the TEM data best, it is possible that if the bicrystal annealing temperature was not high enough,

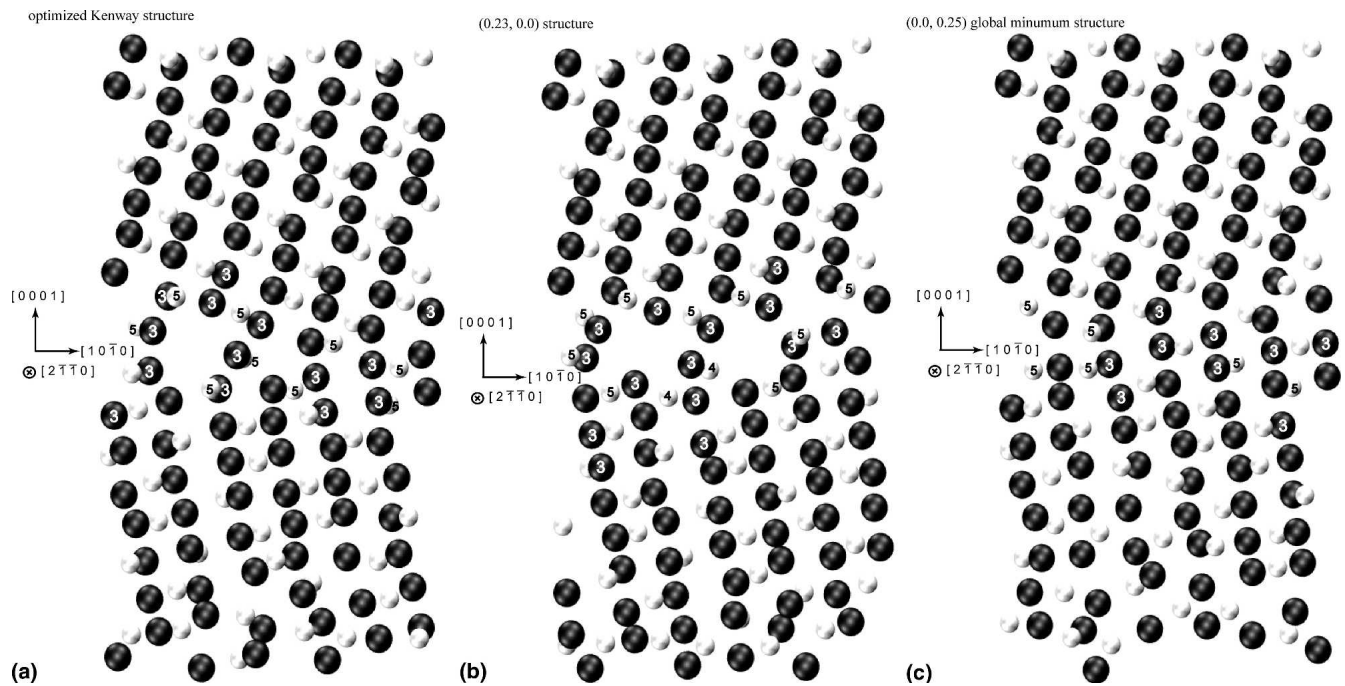


FIG. 3. Side views of low energy GB structures. Aluminum atoms are represented in white and oxygen atoms in black. Coordination numbers are shown on under-coordinated atoms around the GB. Structures are named by the translation vector (numbers in parentheses) from which they originated. The (0.0, 0.25) global minimum structure is obtained by translating the top grain of the grain boundary by the vector (0.0, 0.25, 0.0), expressed in terms of the lattice vectors (a , b , c) of the cell.

the bicrystal might have been trapped in a local minimum with insufficient thermal energy to rearrange to the global minimum. Since it is energetically more stable, our predicted most stable GB structure may form at higher temperatures where kinetic trapping would be unlikely.

The coordination numbers of the atoms at the GB are also displayed in Fig. 3. Not surprisingly, the coordination number is directly related to the size of the voids. More stable structures have a smaller number of under-coordinated atoms in the GB region. Recall that Al and O atoms in bulk α -alumina are hexa- and tetra-coordinated, respectively. To form a GB from a bulk structure costs energy, and in an ionic material like alumina, the cost is directly related to how many ionic bonds have to be broken or disturbed. Structural relaxation upon GB formation plays an important role, as it can enable broken bonds to reform and thereby alleviate void formation.

Electron density changes that occur upon formation of the GB (Fig. 4) give more insight into interfacial bonding and the origin of stability of the lowest energy GB structures. All changes are strongly localized around the GB interface, with localized accumulation of charge across the interface. Transfer of electrons from regions around Al atoms onto O atoms across the GB occurs, while O electron density is depleted, leading to a reorientation of electrons to maximize Al–O bonding and minimize O–O repulsions across the GB. However, significantly more

electron rearrangement occurs in the lowest energy GB structure (0.0, 0.25), producing more ionic bonds across the GB, thereby decreasing the overall energy. Our global minimum structure cannot be separated into regions with distinct bond lengths as clearly as French and co-workers did for the Kenway model. The whole structure rearranges so that the bond length distribution away from the outer slab surfaces is almost uniform. The only feature that distinguishes the GB interface region from the bulk-like region is the presence of a larger number of longer bonds (>2.1 Å) that connect atoms from opposite side of the boundary (Table III). In addition, the total number of bonds at the GB interface is larger for the most stable structure. The Kenway model structure does have more short bonds than the global minimum structure. It is likely that the atoms at GB interface of the Kenway model structure attempt to compensate for their smaller coordination number by forming shorter bonds with neighboring atoms on the same side of the grain boundary. The higher coordination of atoms at the global minimum interface produces a structure more closely resembling bulk alumina, thereby resulting in a lower total energy.

B. Segregation to alumina grain boundaries

The first step toward characterizing diffusion at alumina GBs is the identification of all stable adsorption sites for each species involved. Accordingly, we scanned

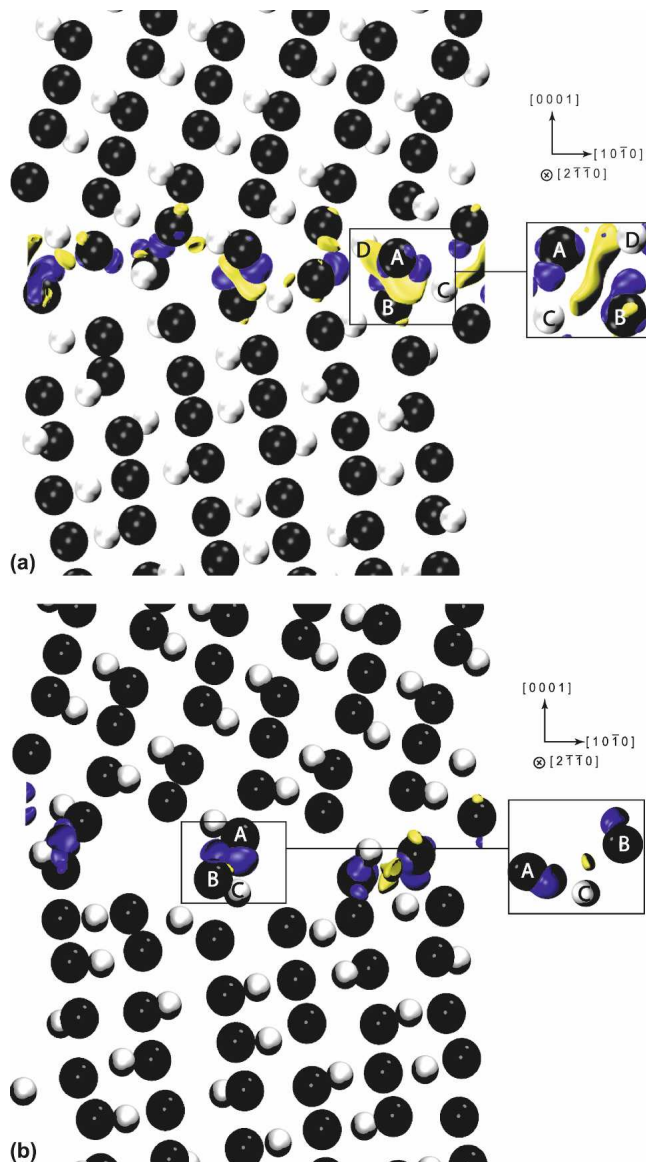


FIG. 4. Electron density changes upon formation of the grain boundary interface for: (a) the (0.0, 0.25) global minimum structure and (b) the (0.23, 0.0) structure. Aluminum atoms are shown as white spheres and oxygen atoms as black. The darker (blue) solid surface represents the $+0.12 \text{ e}/\text{\AA}^3$ isosurface (accumulation in electron density upon formation of the interface), while the lighter (yellow) solid represents the $-0.06 \text{ e}/\text{\AA}^3$ isosurface (depletion of density upon interface formation). The inset contains a magnified and rotated selected region of the GB. To clarify the perspective, the atoms displayed in the inset are labeled with upper-case letters. (color online)

the GB plane for Al, O, Y, and Hf atom adsorption sites by the procedure outlined in Sec. II, now described in more depth for the oxygen atom case. A grid of 27 squares, each with dimensions $\sim 1.5 \text{ \AA} \times 1.2 \text{ \AA}$, was superimposed over the interface of the relaxed (0.0, 0.25) GB. Forty different structures were constructed by placing an O atom at each of the squares' corners and a total energy calculation was performed for each. Then the po-

sition of the adsorbate O atom was optimized for the 13 structures within 7.5 eV of the lowest energy structure. This procedure yielded 10 distinct structures. Then for each of those 10 structures, a full geometry optimization was performed where all ions were allowed to relax. The final sites for oxygen adsorption at the GB are depicted in Fig. 5(a), and their energies relative to the lowest energy structure are given in Table IV. The adsorption sites for oxygen [Fig. 5(a)] are fairly evenly spread over the whole GB interface. The sites differ greatly in energy, with a range of nearly 5 eV. Four sites are found to lie within 2.6 eV of the minimum, but they are not all well-distributed across the cell. This may be why O diffuses more slowly than Al, since O will have to access higher energy minima along its diffusion path.

The same procedure was adopted for mapping the adsorption sites for Al. Ten adsorption sites were identified for Al, and unlike the O adsorption sites, the aluminum sites are not spread over the whole GB interface but are clustered in four distinct regions [Fig. 5(b)]. The energy difference between the lowest and highest energy sites is 5.84 eV, a slightly larger range than found for O (Table IV). However, the five lowest energy Al adsorption sites are closer in energy than found for O. Moreover, these five lowest energy sites are spread more evenly across the unit cell, which may define a facile diffusion pathway for Al.

To reduce the considerable expense of the search for stable adsites, we simplified the procedure for mapping the Y and Hf adsorption sites by first assuming that these metal atoms are likely to prefer to adsorb at sites similar to Al. Therefore, as a starting point, we placed Y and Hf atoms at the ten lowest energy adsorption sites found for Al and then performed full ion relaxations. By doing so, we found five adsorption sites for Y and six sites for Hf. We scanned the GB interface further for additional adsorption sites by attempting to place the Y and Hf atoms in three positions each that would minimize the interaction with Al cations and maximize the interaction with O anions. However, no additional stable adsorption sites were found. Last, Y and Hf atoms were placed at the O adsorption sites and full ion relaxation of the system was performed. Consequently, four additional adsorption sites were found for each atom type, bringing the total number of adsorption sites to nine for Y and 10 for Hf. Based on this more selective scanning procedure, the Hf and Y adsorption sites closely coincide with the Al and some O adsites, as seen in Figs. 5(c)–5(d). Y has four low energy ($< 2.5 \text{ eV}$) adsites that, like O, are not well-distributed across the unit cell, suggesting Y diffusion will be inhibited due to the higher energy diffusion pathway intermediates that would have to be accessed. By contrast, Hf has at least six low energy adsites, spread more evenly across the unit cell, which suggests that Hf diffusion could be more facile than Y diffusion. Of

TABLE III. Al–O bond length distribution of the closest 18 atoms (9 on each side) to the grain boundary for the optimized Kenway model and the optimized (0.0, 0.25) global minimum structure.

	Number of Al–O bonds for each length range (Å)					Total
	<1.80	1.80–1.84	1.84–1.90	1.90–2.10	>2.10	
Kenway model	16	12	23	37	6	94
(0.0, 0.25) structure	10	17	28	31	13	99

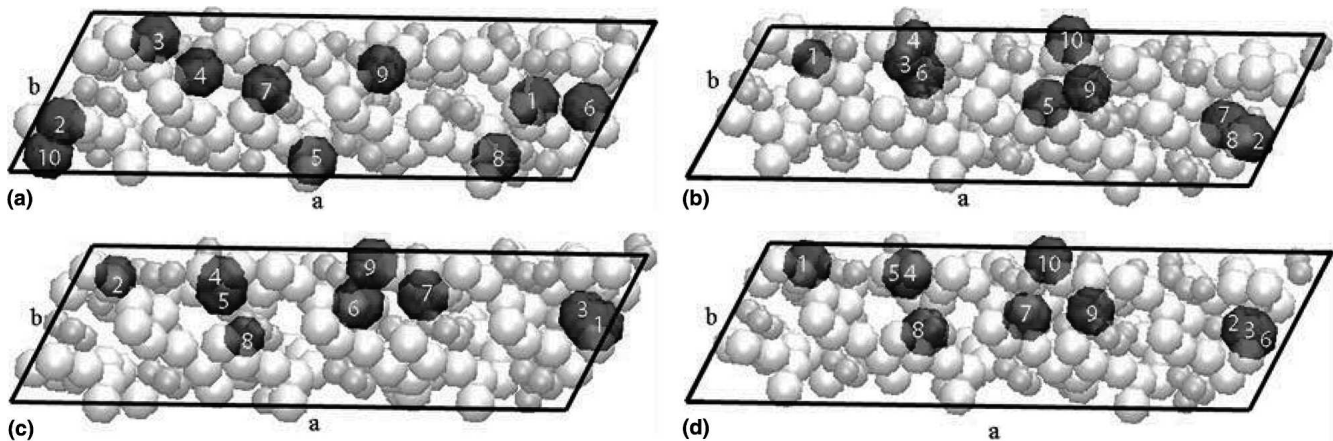


FIG. 5. Stable adsorption sites for: (a) oxygen, (b) aluminum, (c) yttrium, and (d) hafnium. The view is perpendicular to the grain boundary interface plane. The sites are numbered in ascending order from lowest in energy to highest.

TABLE IV. Energies (eV) of the O, Al, Y, and Hf adsorption sites at the global minimum (0.0, 0.25) GB relative to the lowest energy adsorption site for each adsorbate. See Fig. 5 for locations of each site.

Adsorbate	Adsorption sites									
	1	2	3	4	5	6	7	8	9	10
O	0.00	1.44	1.52	1.69	2.6	2.79	3.24	3.42	4.07	4.95
Al	0.00	0.32	1.19	1.78	2.26	2.93	3.16	3.34	3.35	5.84
Y	0.00	0.23	0.23	1.97	2.78	3.62	4.01	4.90	7.36	
Hf	0.00	0.25	0.25	1.23	1.68	2.01	2.64	3.15	4.78	6.88

course, such proposals await verification via diffusion kinetics calculations.⁴⁵

Predicted adhesion energies of the pure and doped GBs are given in Table V, where each dopant atom has been placed at its lowest energy adsite (compare with Table IV and Fig. 5). Two values are reported for each adsorbate, since two possible final states exist after GB fracture: one with the adsorbate on the $(10\bar{1}1)$ surface and the other with the adsorbate on the $(10\bar{1}\bar{1})$ surface. The least negative adhesion energy of each pair of values corresponds to our best estimate of a lower bound on the adhesion energy (shown in boldface), since this represents fracturing into the most stable surfaces. The pure GB adhesion energy is predicted to be -2.4 J/m^2 . Adding Al at the GB weakens it substantially (GB adhesion -1.6 J/m^2), whereas adding O has little effect, slightly increasing the GB adhesion to -2.5 J/m^2 . We predict that all three cations weaken the GB, although the REs Y and Hf do not weaken it as much as Al does. The predicted

adhesion energy for the Y-doped GB is -1.9 J/m^2 , which is larger than for the Al-doped GB, but still less negative than found for the pristine GB. Segregation of Hf has the lowest impact on the GB adhesion energy (-2.2 J/m^2). It is still slightly weaker than the pristine GB, though clearly stronger than both Al- and Y-doped GBs. The slight weakening of the GB by the presence of a segregated Y atom was also predicted by Elsässer et al.,²⁹ who found that doping a twin GB with Y resulted in a slightly lower interfacial work of separation than a pristine GB.

To understand the differences in GB adhesion found for Al, Y, and Hf, we compare bonding characteristics of the three GB unit cells and to pure metal oxide properties (Table VI). All dopants (Al, Y, and Hf) form bonds to neighboring oxygens with lengths very similar to those found in their respective oxides (Al_2O_3 , Y_2O_3 , and HfO_2). The difference is that Y and Hf form five bonds with O atoms at the GB, whereas the extra Al is only tetracoordinated at the GB. All three are

TABLE V. Adhesion energies (J/m^2) of the global minimum $\Sigma 11$ grain boundary structure with and without adsorbates. Two values are reported for each adsorbate, depending on which surface the adsorbate stayed upon fracture of the grain boundary. The values in boldface are the least negative adhesion energies of each pair, providing a lower bound to the adhesion energy.

Adsorbate	Adsorption position	Adhesion energies (J/m^2)
Al	(10 $\bar{1}\bar{1}$)	-1.6
Al	(10 $\bar{1}\bar{1}$)	-1.7
O	(10 $\bar{1}\bar{1}$)	-2.7
O	(10 $\bar{1}\bar{1}$)	-2.5
Y	(10 $\bar{1}\bar{1}$)	-2.1
Y	(10 $\bar{1}\bar{1}$)	-2.0
Hf	(10 $\bar{1}\bar{1}$)	-2.2
Hf	(10 $\bar{1}\bar{1}$)	-2.3
pure		-2.4

undercoordinated relative to their pure oxides. Both Y and Al are hexacoordinated in their corundum structure, and the Hf is heptacoordinated in its monoclinic ground state. The lower coordination of the extra Al may be the origin of the significantly reduced GB adhesion for Al doping. Trends in metal-oxo bond strengths also help explain the adhesion trends observed. It is well known that early transition metals form very strong metal-oxo bonds.⁴⁶ In particular, Hf forms the strongest bonds to oxygen, with Y second, and Al weakest (albeit still very strong). Thus, the combination of a large number of stronger metal-oxo bonds produces the largest GB adhesion for Hf, less for Y, and least for Al.

The reduction in GB adhesion upon addition of atoms appears to be due to relative changes in overall coordination numbers at the GB upon cleavage. We predict that one less metal-oxygen bond is broken upon cleavage of GBs containing a segregated atom, compared to the pristine GB. The grain surfaces with adsorbates are able to retain more metal-oxygen bonds by structural rearrangement, leading to extra stability of the GB surfaces with adsorbates. The net result is that pristine GB has a larger adhesion energy than the doped ones. However, this result could very well be very specific to the type of GB and the type of adsorbate involved.

Last, we evaluated the tendency for multiple REs to segregate to the GB (Table VII). We predict that it is thermodynamically favorable to segregate up to 5 yttrium atoms per unit cell to the GB (0.83 ML). Recall that the

segregation energy quantifies the preference for the RE to reside at the GB versus in the bulk, with a negative value meaning that it is exothermic to move the RE from the bulk to the GB. We predict similar segregation energies for the first, second, and third segregated yttrium atoms: -0.59 , -0.51 , and -0.48 J/m^2 , respectively. Surprisingly, a sharp increase in the segregation energy is predicted for adding a fourth Y atom (-0.90 J/m^2) due to a change in structure of the GB, where the Y atoms push the grains further apart to maximize Y–O bonding on either side of the GB. The segregation energy for the fifth Y atom drops to -0.32 J/m^2 , where the structure remains similar to the case with four Y. We were not successful in obtaining an optimized structure with six Y atoms segregated to the GB, suggesting that 0.83 ML Y may be the saturation coverage.

The segregation energies for hafnium indicate a slightly different behavior. The first and the second hafnium atoms show a significant preference for segregation to the GB, with predicted segregation energies of -0.38 J/m^2 and -0.79 J/m^2 , respectively. However, the predicted segregation energies for the third and fourth hafnium atoms are only -0.13 J/m^2 and -0.03 J/m^2 . Therefore, fewer Hf than Y atoms are likely to segregate to the GB, since the preference of Hf atoms to reside at the GB versus in the bulk is roughly thermoneutral beyond 2 Hf atoms/unit cell (0.33 ML). Thus we find the atom with the larger ionic radius (Y) has an overall higher propensity for segregation to the grain boundary than the one with the smaller ionic radius (Hf), consistent with a direct relationship between ionic radius and propensity for segregation to the GB found earlier by Elsässer and coworkers.²⁹

The different segregation behavior for Y and Hf can be understood further by examining the Al_2O_3 – Y_2O_3 and Al_2O_3 – HfO_2 phase diagrams. Yttria does not have high solubility in alumina and readily precipitates out as a compound (YAG: $3\text{Y}_2\text{O}_3 \cdot 5\text{Al}_2\text{O}_3$) in the alumina solid solution even at low concentration.⁴⁷ Hafnia, on the other hand, does not form a compound with alumina.⁴⁸ After the concentration of hafnia reaches the solubility limit, two coexisting solid solutions are obtained. This indicates that it is more energetically favorable for yttrium atoms to cluster into YAG particles, whereas hafnium atoms would likely be distributed more evenly

TABLE VI. Bond lengths, $R(\text{M-O})$, in Å, between adsorbed Hf, Y, or Al atoms and neighboring O atoms at the global minimum $\Sigma 11$ grain boundary structure. Experimental bond lengths (Å) in pure HfO_2 ,⁵⁶ Y_2O_3 ,⁵⁷ and α - Al_2O_3 ,⁵⁸ as well as experimental metal-O diatomic bond enthalpies $D_{298}(\text{M-O})$ at 298 K (kJ/mol)⁵⁹ are provided for comparison.

Adsorbate	R(M-O) at GB (DFT-GGA)					R(M-O) in bulk oxide (experimental)	$D_{298\text{K}}(\text{M-O})$ (experimental)
	2.05	2.10	2.20	2.22	2.24	2.04–2.25	801
Hf	2.05	2.10	2.20	2.22	2.24	2.04–2.25	801
Y	2.29	2.29	2.30	2.32	2.37	2.2–2.32	719
Al	1.82	1.89	1.89	1.99		1.87, 1.97	511

TABLE VII. Segregation energies (J/m^2) for the segregation of each additional RE atom to the GB.

Segregated atom	Segregation energies (eV)				
	1st	2nd	3rd	4th	5th
Y	-0.59	-0.51	-0.48	-0.90	-0.32
Hf	-0.38	-0.79	-0.13	-0.03	

throughout the alumina. Thus, it is likely that hafnium atoms move into the bulk once the GB interface is saturated, while more yttrium atoms can bond at the interface forming a “local” compound.

IV. DISCUSSION

The minimum energy structure of the $\Sigma 11$ GB obtained here differs from the one suggested by Rühle and coworkers (the Kenway model).²⁵ According to our all-electron DFT-GGA calculations, the structure they report is not the global minimum and is just one of many minima on the GB sliding potential energy surface. The discrepancy could be due to a lack of transferability of the pairwise additive potentials derived from bulk alumina, which may not be appropriate for describing the undercoordinated structure of a GB. We find the Kenway model is ~ 5 eV/unit cell above the global minimum structure, with bonding and an ion distribution in the GB region that differs significantly from the lowest energy structure. The global minimum structure has more bonds across the GB, resulting in a smaller number of undercoordinated atoms and the ions are more uniformly spaced, producing smaller void spaces. At the high temperatures at which the α -alumina layer grows in TBCs, it is very likely that the thermodynamically most stable structure will form (kinetic barriers to rearrangement can be overcome). Such rearrangements to denser structures also have important implications for segregation and diffusion of ions along alumina GBs: dense structures are likely to limit both.

The GB structure Rühle and coworkers proposed with their theoretical methodology agrees rather well with their HRTEM micrographs. Since our higher level calculations contradict their findings, it may simply be that their procedure of forming the bicrystal seed does not guarantee production of the lowest GB structure. Rühle and coworkers obtain the bicrystal by cutting single crystals, putting them together and annealing them in an argon atmosphere. It is unclear from their experimental procedure at what temperature the bicrystal was held and if it was high enough to access the most stable state.

The mapping of O, Al, Y, and Hf adsorption sites at the $\Sigma 11$ $(10\bar{1}\bar{1})\parallel(10\bar{1}\bar{1})$ GB has unveiled significant differences in their adsorption behavior. Assuming that diffusion proceeds via these stable sites, we can speculate

on how Al and O diffusion may be affected by REs. First, we find that O, Al, Y, and Hf each have at least nine stable adsorption sites. However, the existence of additional sites cannot be excluded, including regions slightly away from the GB interface. By analyzing the adsorption site maps (Fig. 5), we observe that the oxygen adsites are uniformly distributed along the interface, while Al, Y, and Hf sites tend to be more concentrated in certain regions of the interface. To the best of our ability to determine them, the preferred adsorption sites for Al, Y, and Hf are spatially very close to each other (Fig. 6). Thus, segregation of REs to the GB may very well affect the availability of Al adsorption sites, perhaps blocking the most direct diffusion pathway for Al. The diffusion rate of Al should experience a significant decrease, as the accessibility of alternative diffusion pathways seems very limited. This is consistent with the dynamic-segregation theory put forward by Pint,¹⁶ which suggests REs inhibit diffusion of Al. The oxygen diffusion rate should also decrease, as some of the oxygen adsorption sites are in the vicinity of RE adsorption sites. This should prompt partial site-blocking or possibly promote bonding of the oxygen to the undercoordinated RE atoms, perhaps trapping oxygen. However, the effect on the O diffusion rate should be less than for Al because of the rather uniform distribution of O adsites throughout the GB interface. It seems that even when a RE adsorbate is present, oxygen would have alternative diffusion pathways available. This is entirely consistent with the observation that REs convert alumina growth from Al-diffusion controlled to O-diffusion controlled,⁴⁹ and that the growth is slowed, but not stopped, in the presence of REs.¹⁹

The segregation energies calculated for yttrium show that it is energetically favorable to have up to five yttrium atoms segregated simultaneously on the GB (0.83 ML). This means that a rather high concentration of yttrium atoms can be achieved at this grain boundary, which would further lower the diffusion rates of Al and O atoms. Of course, in reality, the actual concentration of GB-segregated yttrium atoms might not correspond to this high value. Unlike our model, where the $\Sigma 11$ unit cell is infinitely repeated along the interface plane, a real system contains a large number of different types of GBs. Bouchet et al. studied the segregation distribution of Y

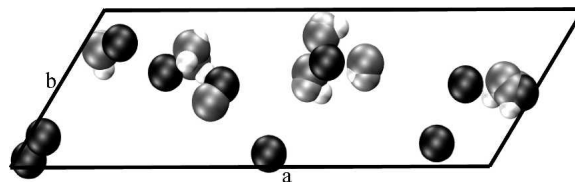


FIG. 6. Adsorption sites for Al (atoms in white), O (atoms in black), Y (atoms in dark gray), and Hf (atoms in light gray) on the grain boundary interface plane in one unit cell.

atoms along a twin rhombohedral α -alumina grain boundary slightly deviated from perfect lattice coincidence to create a high concentration of large defects (dislocations).⁵⁰ They found that Y atoms do not segregate to the pristine parts of the grain boundary but diffuse to defects instead. Chi and Gu studied the segregation of Si and Ti at 20 different alumina bicrystals using HRTEM and energy-dispersive x-ray spectroscopy (EDX) techniques.⁵¹ They found that segregation of both Si and Ti is enhanced at GBs with disordered interfaces (7–30 atoms/nm²) compared to low-angle GBs (1–3 atoms/nm²). Thus, if relatively ordered and low-angle GBs like the Σ 11 are adjacent to high-angle GBs in a real sample, it would probably be energetically more favorable for the yttrium atoms to diffuse to these higher-angle GBs, resulting in a lower yttrium concentration at Σ 11 GBs.

Reactive elements may have an additional effect on TGO stability besides blocking Al cation diffusion along GBs, thereby slowing down oxide growth. It has been proposed that GB sliding plays a very important role in creep of α -alumina.^{52,53} HRTEM experiments analyzed with EDX⁵⁴ demonstrated that yttrium-doped α -alumina is more resistant to GB sliding. A PAW-DFT-GGA study⁵⁵ suggested that segregation of Y to a symmetrical tilt Σ 31 [0001] GB would cause a slight increase in the number of bonds at the interface. In addition to that effect, it was suggested that the Y–O bonds are more covalent and stronger than Al–O bonds, resulting in strengthening of the GB, preventing it from sliding. We do not observe a strengthening effect of the segregated REs at this GB. Although adding Y and Hf to the GB is energetically favorable relative to Y and Hf impurities residing in bulk alumina, we find they decrease the GB adhesion energy because REs stabilize the separated surfaces even more. We conclude that adhesion energies alone do not provide direct insights into creep inhibition in RE-doped aluminas, and that further work is needed to elucidate the GB sliding mechanism. However, the strength of the metal–oxygen bond does seem to play an important role. The extent to which the GB adhesion energy is decreased is directly related to the strength of the metal–oxygen bonds the segregated atom can form (Table VI). Thus, a dopant that forms weaker bonds to oxygen could potentially have an undesirable effect on creep prevention because its beneficial effects as a site-blocker for diffusion could be offset by the weakening of the GB.

V. SUMMARY

We have used periodic PAW-DFT-GGA calculations to characterize the structure and bonding of the α -alumina Σ 11 (10 $\bar{1}$ 1)|(10 $\bar{1}$ $\bar{1}$) GB, as a model for understanding atomic processes occurring at alumina GBs in the thermally grown oxide layer of thermal barrier coat-

ings. We selected this particular GB because it had been characterized previously both experimentally and theoretically.

We found new lower energy structures differing from one suggested previously in the literature more than a decade ago. Due to use of a higher level of theory and the more meticulous searching method used, it is likely that the GB characterization presented here is more reliable and in particular more relevant to GBs growing under high-temperature oxidation conditions. The atoms at the GB interface in our structure are found to resemble less a surface crystal structure and instead appear more bulk-like.

Rühle and coworkers had previously suggested a structure for the Σ 11 GB by a combination of HRTEM and theory that conserves the basic shape of both crystals making up the GB but contains a significant number of under-coordinated atoms in the GB region and, as a result, has a notable amount of void space. The global minimum structure we found contains considerably less void space, since the atoms at the interface rearrange themselves to maximize the number of bonds present. Such a structure with less undercoordinated bonds is energetically more stable and more probable, especially at the high temperatures at which the alumina grows in and is subjected to in TBC applications.

The results of our study of the adsorption of Al, O, Y, and Hf atoms at this GB support the dynamic-segregation theory put forward by Pint. The segregation of REs like Y and Hf to the GB should hinder the diffusion of Al cations by blocking their preferred adsorption sites. The presence of yttrium and hafnium at the GB had the effect of slightly decreasing the GB adhesion energy, which is not consistent with the observation of reduced creep upon Y doping of alumina, indicating that adhesion energies alone are not sufficient to explain the creep inhibition properties of RE. More detailed calculations of GB sliding in the presence and absence of REs, as well as diffusion of ions along this GB will be reported elsewhere.⁴⁵

In closing, we note that the high symmetry of this particular GB may not make it a particularly realistic representative of the large number of possible GBs formed upon oxidation of the NiAl bond coat, but our intention was to draw only qualitative conclusions that we hope will be somewhat general. More theoretical work is needed to confirm that the trends we observe can be generalized to more disordered grain boundaries, which are more likely to occur in an actual oxide scale.

ACKNOWLEDGMENTS

We are grateful to the Air Force Office of Scientific Research (AFOSR) for support of this work and Maui High Performance Supercomputing Center and Naval Oceanographic Office (NAVO) for the use of their

supercomputers. B. Hinnemann and E.A. Carter thank C. Elsässer, M. Harmer, and H. Chan for useful discussions.

REFERENCES

- N.P. Padture, M. Gell, and E.H. Jordan: Materials science—Thermal barrier coatings for gas-turbine engine applications. *Science* **296**, 280 (2002).
- G.W. Goward: Progress in coatings for gas turbine airfoils. *Surf. Coat. Technol.* **108–109**, 73 (1998).
- A.G. Evans, D.R. Mumm, J.W. Hutchinson, G.H. Meier, and F.S. Petit: Mechanisms controlling the durability of thermal-barrier coatings. *Prog. Mater. Sci.* **46**, 55 (2001).
- B.A. Pint, J.R. Martin, and L.W. Hobbs: O-18/SIMS characterization of the growth-mechanism of doped and undoped α -Al₂O₃. *Oxid. Met.* **39**, 167 (1993).
- M. Le Gall, A.M. Huntz, B. Lesage, C. Monty, and J. Bernardini: Self-diffusion in α -Al₂O₃ and growth-rate of alumina scales formed by oxidation—Effect of Y₂O₃ doping. *J. Mater. Sci.* **30**, 201 (1995).
- D. Prot and C. Monty: Self-diffusion in α -Al₂O₃. 2. Oxygen diffusion in ‘undoped’ single crystals. *Philos. Mag. A* **73**, 899 (1996).
- M. Le Gall, A.M. Huntz, B. Lesage, and C. Monty: Self-diffusion in α -Al₂O₃. 3. Oxygen diffusion in single crystals doped with Y₂O₃. *Philos. Mag. A* **73**, 919 (1996).
- D. Prot, M. Le Gall, B. Lesage, A.M. Huntz, and C. Monty: Self-diffusion in α -Al₂O₃. 4. Oxygen grain-boundary self-diffusion in undoped and yttria-doped alumina polycrystals. *Philos. Mag. A* **73**, 935 (1996).
- J. Pan, J. Oijerholm, A.B. Belonoshko, A. Rosengren, and C. Leygraf: Self-diffusion activation energies in α -Al₂O₃ below 1000 °C—Measurements and molecular dynamics calculation. *Philos. Mag. Lett.* **84**, 781 (2004).
- P. Fielitz, G. Borchardt, M. Schmucker, H. Schneider, and P. Willich: Measurement of oxygen grain-boundary diffusion in mullite ceramics by SIMS depth profiling. *J. Am. Ceram. Soc.* **87**, 2232 (2004).
- J.H. Harding, K.J.W. Atkinson, and R.W. Grimes: Experiment and theory of diffusion in alumina. *J. Am. Ceram. Soc.* **86**, 554 (2003).
- A.B. Belonoshko, A. Rosengren, Q. Dong, G. Hultquist, and C. Leygraf: First-principles study of hydrogen diffusion in α -Al₂O₃ and liquid alumina. *Phys. Rev. B* **69**, 024302 (2004).
- J. Carrasco, N. Lopez, and F. Illas: First principles analysis of the stability and diffusion of oxygen vacancies in metal oxides. *Phys. Rev. Lett.* **93**, 225502 (2004).
- Y. Oishi and W.D. Kingery: Self-diffusion of oxygen in single crystal and polycrystalline aluminum oxide. *J. Chem. Phys.* **33**, 480 (1960).
- K. Kitazawa and R.L. Coble: Chemical diffusion in polycrystalline Al₂O₃ as determined from electrical-conductivity measurements. *J. Am. Ceram. Soc.* **57**, 250 (1974).
- B.A. Pint: Experimental observations in support of the dynamic-segregation theory to explain the reactive-element effect. *Oxid. Metal.* **45**, 1 (1996).
- I.G. Wright and B.A. Pint: Bond coating issues in thermal barrier coatings for industrial gas turbines. *Proc. IMechE* **219**, 101 (2005).
- J. Cho, C.M. Wang, H.M. Chan, J.M. Rickman, and M.P. Harmer: Grain boundary chemistry and creep resistance of oxide ceramics. *Acta Mater.* **47**, 4197 (1999).
- P.Y. Hou: Impurity effects on alumina scale growth. *J. Am. Ceram. Soc.* **86**, 660 (2003).
- J.D. French, J. Zhao, M.P. Harmer, H.M. Chan, and G.A. Miller: Creep of duplex microstructures. *J. Am. Ceram. Soc.* **77**, 2857 (1994).
- J. Cho, M.P. Harmer, H.M. Chan, J.M. Rickman, and A.M. Thompson: Effect of yttrium and lanthanum on the tensile creep behavior of aluminum oxide. *J. Am. Ceram. Soc.* **80**, 1013 (1997).
- M. Rühle: Structure and composition of metal-ceramic interfaces. *J. Eur. Ceram. Soc.* **16**, 353 (1996).
- T. Höche, P.R. Kenway, H-J. Kleebe, M.W. Finnis, and M. Rühle: The structure of special grain-boundaries in α -Al₂O₃. *J. Phys. Chem. Solids* **55**, 1067 (1994).
- G. Richter and M. Rühle: Quantitative HRTEM investigations of a symmetrical tilt Sigma 11 grain boundary with two different grain boundary planes in α -Al₂O₃. *Interface Sci.* **12**, 197 (2004).
- T. Höche, P.R. Kenway, H-J. Kleebe, M. Rühle, and P.A. Morris: High-resolution transmission electron-microscopy studies of a near Σ 11 grain boundary in α -Al₂O₃. *J. Am. Ceram. Soc.* **77**, 339 (1994).
- P.R. Kenway: Calculated structures and energies of grain-boundaries in α -Al₂O₃. *J. Am. Ceram. Soc.* **77**, 349 (1994).
- S-D. Mo, W-Y. Ching, and R.F. French: Electronic structure of a near Σ 11 *a*-axis tilt grain boundary in α -Al₂O₃. *J. Am. Ceram. Soc.* **79**, 627 (1996).
- H. Müllejans and R.H. French: Interband electronic structure of a near- Σ 11 grain boundary in α -Al₂O₃ determined by spatially resolved valence electron energy-loss spectroscopy. *J. Phys. D: Appl. Phys.* **29**, 1751 (1996).
- C. Elsässer and A.G. Marinopoulos: Substitutional cation impurities in α -Al₂O₃: Ab-initio case study of segregation to the rhombohedral twin boundary. *Acta Mater.* **49**, 2951 (2001).
- S. Fabris and C. Elsässer: Σ 13 (1014) twin in α -Al₂O₃: A model for a general grain boundary. *Phys. Rev. B* **64**, 245117 (2001).
- S. Fabris and C. Elsässer: First-principles analysis of cation segregation at grain boundaries in α -Al₂O₃. *Acta Mater.* **51**, 71 (2003).
- J. Cho, J.M. Rickman, H.M. Chan, and M.P. Harmer: Modeling of grain-boundary segregation behavior in aluminum oxide. *J. Am. Ceram. Soc.* **83**, 344 (2000).
- P. Hohenberg and W. Kohn: Inhomogeneous electron gas. *Phys. Rev. B* **136**, 864 (1964).
- W. Kohn and L.J. Sham: Self-consistent equations including exchange and correlation effects. *Phys. Rev.* **140**, A1133 (1965).
- G. Kresse and J. Hafner: Ab initio molecular dynamics for open-shell transition-metals. *Phys. Rev. B* **48**, 13115 (1993).
- G. Kresse and J. Fürthmüller: Efficient iterative schemes for ab initio total-energy calculations using a plane-wave basis set. *Phys. Rev. B* **54**, 11169 (1996).
- G. Kresse and J. Fürthmüller: Efficiency of ab-initio total energy calculations for metals and semiconductors using a plane-wave basis set. *Comput. Mater. Sci.* **6**, 15 (1996).
- P.E. Blöchl: Projector augmented-wave method. *Phys. Rev. B* **50**, 17953 (1994).
- G. Kresse and D. Joubert: From ultrasoft pseudopotentials to the projector augmented-wave method. *Phys. Rev. B* **59**, 1758 (1999).
- J.P. Perdew, K. Burke, and M. Erzerhof: Generalized gradient approximation made simple. *Phys. Rev. Lett.* **77**, 3865 (1996).
- H.J. Monkhorst and J.D. Pack: Special points for Brillouin-zone integrations. *Phys. Rev. B* **13**, 5188 (1976).
- B. Hinnemann and E.A. Carter: Adsorption of Al, O, Hf, Y, Pt, and S atoms on α -Al₂O₃ (0001). *J. Phys. Chem. C* **111**, 7105 (2007).
- R. Voytovych, I. MacLaren, M.A. Gülgün, R.M. Cannon, and M. Rühle: The effect of yttrium on densification and grain growth in α -Al₂O₃. *Acta Mater.* **50**, 3453 (2002).

44. C.M. Wang, G.S. Cargill III, H.M. Chan, and M.P. Harmer: Structural features of Y-saturated and supersaturated grain boundaries in alumina. *Acta Mater.* **48**, 2579 (2000).
45. I. Milas and E.A. Carter (unpublished).
46. E.A. Carter and W.A. Goddard III: Early-transition versus late-transition metal-oxo bonds—The electronic structure of VO^+ and RuO^+ . *J. Phys. Chem.* **92**, 2109 (1988).
47. T. Noguchi and M. Mizuno: *Kogyo Kagaku Zasshi* **70**, 839 (1967).
48. O. Fabrichnaya and C. Mercer: Phase relations in the HfO_2 – Y_2O_3 – Al_2O_3 system. *Calphad* **29**, 239 (2005).
49. K.P.R. Reddy, J.L. Smialek, and A.R. Cooper: O-18 tracer studies of Al_2O_3 scale formation on NiCrAl alloys. *Oxid. Met.* **17**, 429 (1982).
50. D. Bouchet, S. Lartigue-Korinek, R. Molins, and J. Thibault: Yttrium segregation and intergranular defects in alumina. *Philos. Mag. A* **86**, 1401 (2006).
51. M.F. Chi and H. Gu: Comparison of segregation behaviors for special and general boundaries in polycrystalline Al_2O_3 with SiO_2 – TiO_2 impurities. *Inter. Sci.* **12**, 335 (2004).
52. O.A. Ruano, J. Wadsworth, and O.D. Sherby: Deformation of fine-grained alumina by grain boundary sliding accommodated by slip. *Acta Mater.* **51**, 3617 (2003).
53. J.N. Wang: An investigation of the deformation mechanism in grain size-sensitive newtonian creep. *Acta Mater.* **48**, 1517 (2000).
54. K. Matsunaga, H. Nishimura, H. Muto, T. Yamamoto, and Y. Ikuhara: Direct measurements of grain boundary sliding in yttrium-doped alumina bicrystals. *Appl. Phys. Lett.* **82**, 1179 (2003).
55. J.P. Buban, K. Matsunaga, J. Chen, N. Shibata, W.Y. Ching, T. Yamamoto, and Y. Ikuhara: Grain boundary strengthening in alumina by rare earth impurities. *Science* **311**, 212 (2006).
56. J. Adams and M.D. Rogers: The crystal structure of ZrO_2 and HfO_2 . *Acta Crystall.* **12**, 951 (1959).
57. Y. Repelin, C. Proust, E. Husson, and J.M. Beny: Vibrational spectroscopy of the c-form of yttrium sesquioxide. *J. Solid State Chem.* **118**, 163 (1995).
58. L.W. Finger and R.M. Hazen: Crystal-structure and compression of ruby to 46 kbar. *J. Appl. Phys.* **49**, 5823 (1978).
59. *CRC Handbook of Chemistry and Physics*, 79 ed., edited by D.R. Linde and H.P.R. Frederikse (CRC Press, Boca Raton, FL, 1999).